Passive separation control by acoustic resonance

S. L. Yang · G. R. Spedding

Abstract At transitional Reynolds numbers, the laminar boundary layer separation and possible reattachment on a smooth airfoil, or wing section, are notoriously sensitive to small variations in geometry or in the fluid environment. We report here on the results of a pilot study that adds to this list of sensitivities. The presence of small holes in the suction surface of an Eppler 387 wing has a transformative effect upon the aerodynamics, by changing the mean chordwise separation line location. These changes are not simply a consequence of the presence of the small cavities, which by themselves have no effect. Acoustic resonance in the backing cavities generates tones that interact with intrinsic flow instabilities. Possible consequences for passive flow control strategies are discussed together with potential problems in measurements through pressure taps in such flow regimes.

1 Introduction

An emerging generation of practical micro-air vehicles (MAVs) operates at flight speeds and characteristic length scales that bring them into an especially challenging flight regime, where abrupt changes in flight performance can result from very small, and often uncontrolled, changes in the geometry and/or environmental conditions. For example, [16, 21, 22] show data from a number of facilities with factors of two variations in sectional drag coefficient (c_d, with c_l the corresponding sectional lift coefficient) at moderate, pre-stall, geometric angles of attack, α.

S. L. Yang (✉) · G. R. Spedding
Department of Aerospace and Mechanical Engineering,
University of Southern California, Los Angeles, CA 90089, USA
e-mail: shanling.yang@usc.edu

Experimental difficulties are exacerbated because the relatively small forces (of mN or less) are difficult to measure directly on standard force balance equipment, so scanning arrays of pitot tubes are used to measure the streamwise momentum defect to estimate the profile drag, and it is possible that variations in local sectional properties across the span could increase the measurement uncertainty greatly. Yang and Spedding [29] showed that at a chord-based Reynolds number, $Re \approx 8 \times 10^4$ ($Re = Uc/\nu$, where U is the flight speed, c is the wing chord, and ν is the kinematic viscosity), there were measurable variations in c_d across the span of an E387 wing, but that they were not of sufficient magnitude to account for disparities in the literature.

The E387 airfoil is a well-studied airfoil, originally designed for sailplanes at moderate Re ($\geq 2 \times 10^5$). The E387 has been referred to as the low Re calibration standard [24], since at low Re ($< 1 \times 10^5$), it experiences laminar separation without reattachment, laminar separation with turbulent reattachment, and turbulent trailing edge separation. Although these phenomena that occur at low Re do not make the E387 a strong candidate for practical MAV design, it can be used as a testbed for the study of transitional phenomena where small variations can have a large dynamical effect.

Performance data for the same E387 wing used in [29] that included a lower range of Re values than customary in typical wind tunnel studies (Re ranged from $1-8 \times 10^4$) [26, 28] showed that at moderate $\alpha = 4°-8°$, the flow can be in either one of the two states. In one state, a lower envelope of $c_l(c_d)$ curves marks the performance characteristics where trailing edge separation gradually moves forward on the wing, and c_d increases rapidly for $\alpha > 4°$, while c_l rises rather slowly to maximum values of about 0.8. This low-lift state will be referred to as SI. In a second state, the initial separation point has moved close to the leading edge, but the flow reattaches

before the trailing edge. This high-lift state will be referred to as SII. Consequently, at any given c_d, c_l has a value about 40 % higher than in SI. The lower-lift envelope of SI is occupied by all points at $Re \leq 2 \times 10^4$, and the upper envelope of SII is a characteristic of polars for $Re \geq 8 \times 10^4$. In between, and at interim $4° \leq \alpha \leq 10°$, the flow can separate either close to the leading edge, or further aft, and the global aerodynamic force coefficients can match with either state SI or SII. The state switch SI–SII has hysteresis, so the flow at any α depends on the time history, or previous state.

The peculiar (when contrasted with the usual, simple C-shape curves at higher Re) shape of the lift-drag polar of the E387 at intermediate Re is not actually restricted to this single profile shape, but is quite characteristic of a class of airfoils that have smooth rounded leading edges with some minimum profile thickness. Seventy-four of 94 airfoils in [16, 21, 22] at $Re < 10^5$ have this polar shape, with non-unique values of c_l over some range of c_d, and 18 of 31 profiles compiled by [23] have it too. The polar shape is due to the abrupt forward movement of the separation line, with an accompanying reduction in c_d and increase in c_l [17]. Absent from any other evidence at these Re, it is reasonable to assume that the same dynamics occur in all these airfoil/wing systems.

The acute sensitivity of an airfoil configuration at intermediate Re (E61 at $Re = [25, 35, 50, 60] \times 10^3$) was noted by Grundy et al. [13], who also showed a dependence on the background acoustic environment. It was further demonstrated that the most effective forcing frequencies coincided with resonant modes in the tunnel test section and therefore that sensitivity to ambient acoustic noise will be facility-dependent. The same result was shown in [28], where control of the SI–SII transition and its hysteresis loop around transitional α could be achieved at resonant modes in the tunnel. The spatial distribution of the sound pressure levels was not uniform, but local minima in SPL at the wing location were associated with the most effective forcing frequencies.

In continuation of the acoustic forcing tests reported in [28], the next step in testing the response to acoustic forcing was to embed arrays of small speakers inside the wing profile, and to do that, arrays of small holes were drilled in a wing lid that enclosed cavities to house the speakers. In this short note, we report on how the presence of the holes themselves profoundly changes the properties of the wing, locking the flow onto the high-lift state SII.

2 Materials and methods

2.1 Wing model

The aluminum wing had an Eppler 387 profile section (Fig. 1) with aspect ratio of 6 (span of 54 cm and chord of 9 cm). The wing was custom designed to consist of a base and a lid, which fit together with a tongue-and-groove connection. The wing, which originally started as a solid piece of aluminum, was manufactured by electrical discharge machining wire cutting (wire EDM), which is a thermal mass-reducing process that uses a constantly moving wire to remove material by rapid, controlled and repetitive spark discharges. The removed particles are flushed with a dielectric fluid, which also regulates the discharge and keeps the wire and metal cool. The tolerance on the wire EDM is ±0.05 mm. The lid of the wing was 1 mm thick and contained 180 0.5-mm-diameter holes arranged in six spanwise arrays with 30 holes each. The six spanwise arrays were located at streamwise locations $x/c =$ 0.1, 0.2, 0.3, 0.4, 0.5, 0.6. The base of the wing contained 180 cavities that were aligned with the holes in the lid; these cavities were connected to each other through spanwise channels for wiring and ultimately to an exit port aft of the quarter-chord mount point.

2.2 Experimental setup

Experiments were performed in the low turbulence Dryden wind tunnel at USC, where the empty test section turbulence level is 0.025 % for spectral frequencies between $2 \leq f \leq 200$ Hz in the velocity range $5 \leq U \leq 26$ m/s. Measurements on flow uniformity yielded no more than 0.5 % velocity deviation from the mean for a given cross-section [30]. The wing assembly was mounted vertically to a sting at one wingtip, at the quarter-chord point (Fig. 2). The flow is known to be sensitive to small disturbances (e.g., [16, 18]), and placing the mount point at one tip confines this particular disturbance to a region that at moderate α is dominated by the induced flow of the tip vortex [29] and is therefore not closely associated with determining separation points on the central part of the wing, where most measurements are focused. As noted in the figure, coordinate axes $\{x, y, z\}$ run streamwise, spanwise, and vertically, respectively, with origin at the mid-span leading edge at $\alpha = 0°$. Time-averaged lift and drag forces were measured with a custom force balance with measurement uncertainty of 0.1 mN, described in [17, 26, 30].

2.3 Particle imaging velocimetry

Particle image velocimetry (PIV) was used for the estimation of the velocity components $\{u, w\}$ in $\{x, z\}$. A Continuum Surelite II dual-head Nd:YAG laser generated pulse laser pairs separated by exposure times, $\delta t =$ 100–300 μs. The pulse-pair repetition rate was fixed at 10 Hz. At $Re = 60$ k, $U = 10$ m/s, and a convective time, $c/U \approx 0.01$ s, which is 10 times the sampling rate. Each

Fig. 1 **a** E387 wing with 180 0.5-mm-diameter holes in the 1-mm *thick* lid, and **b** profile view of the lid of the wing
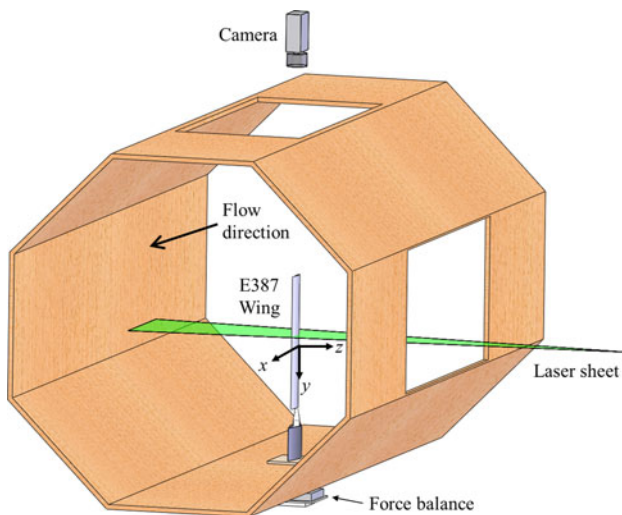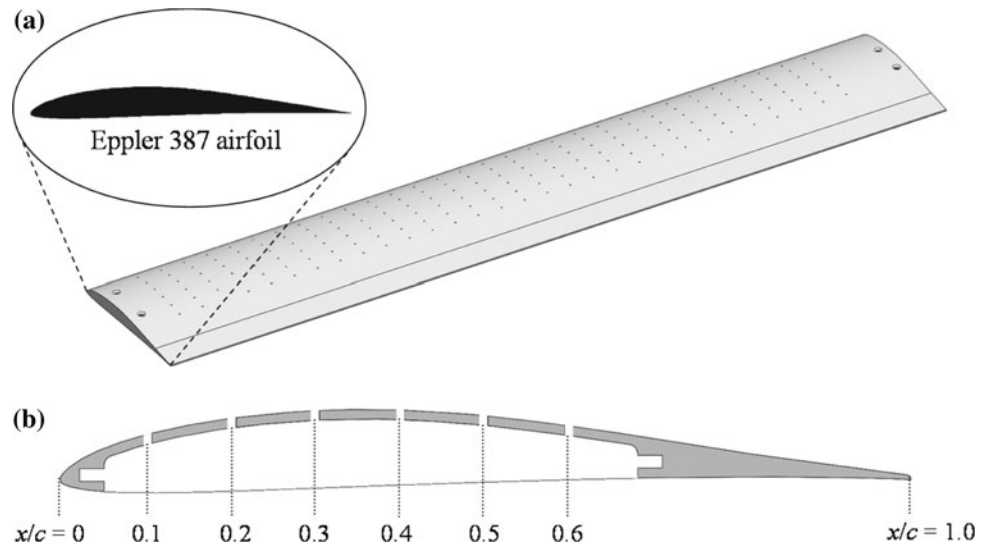

Fig. 2 Wind tunnel setup. (x, y, z) are streamwise, spanwise, and normal directions. Origin is at leading edge and mid-span

velocity field in a sequence can therefore be used for statistical sampling, but not for the resolution of time-varying events. A sequence of convergent-cylindrical–cylindrical lenses converted the two co-linear laser beams into coplanar laser sheets with slowly varying thickness. The flow was seeded with 1 μm smoke particles from a Colt 4 smoke generator and captured by an Imager Pro X 2M (1,648 × 1,214 × 14-bit) camera.

PIV processing was based on the customized CIV algorithms described in [9, 10] in which a smoothed spline interpolated cross-correlation function was directly fit with the equivalent splined auto-correlation functions from the same data. Obviously, wrong vectors that passed by an automated rejection criterion were manually removed and the raw displacement vector field was reinterpolated back

onto a complete rectangular grid with the same smoothing spline function [25]. The spline coefficients are differentiated analytically to generate velocity gradient data. The uncertainty is fixed in fractions of a pixel, and when rescaled to the test conditions reported here, expected uncertainties are 0.5–5 % in $\{u, w\}$ and ≈ 10 % in gradient-based quantities, such as the spanwise vorticity:

$$\omega_y = \frac{\partial w}{\partial x} - \frac{\partial u}{\partial z}.$$

ω_y is displayed on a discrete colorbar whose step size matches the measurement uncertainty.

2.4 The imperfect test environment

No physical experiment conforms perfectly to its nominal configuration. Here, we document some of the departures from ideal test conditions. Comparative tests indicate that none of these are critical in influencing the basic phenomena described here, but flows at transitional Re are known to be sensitive to a number of sometimes poorly- or partially controlled environmental variables, and it is useful to at least know what some are.

2.4.1 Background acoustic environment

This paper concerns the sensitivity of wing aerodynamics to acoustic perturbations that occur in a background non-zero acoustic ambient. No special attempts were made to modify the tunnel geometry to tailor the background acoustics, either from obvious sources (such as the downstream fan) or from reflections at test section walls. The tunnel is not an anechoic chamber. Acoustic power spectra were measured with a shielded 1/4" B&K microphone oriented normal to the mean flow direction. Each power

spectrum is an average of at least 10 individual spectra, each taken from 10,000 samples and sampled at 10,000 Hz. The acoustic power spectra with and without flow in the empty test section were measured at the equivalent mid-span, quarter chord, and top surface of the wing (with no wing present) and are shown in Fig. 3.

A constant peak at 300 Hz, with no wind on, measures the background environmental noise. Though striking by itself, its amplitude is small when compared with peaks that appear when the wind is on. These include an increase in the 300 Hz component and another at about 360 Hz. These will come from the fan noise combined with self-noise of the microphone head. Though shielded, zero self-noise cannot be obtained. The background acoustic spectrum is subtracted from all subsequent spectra.

2.4.2 Wing tip deflections

The maximum absolute deflection amplitude, z', was measured at the free wing tip ($y/b = -1.0$) from image sequences taken from the camera mounted on top of the wind tunnel. $z'(\alpha)$ was measured for $Re = 40$ and 60 k for the wing with all holes covered (the solid wing), and results are shown in Fig. 4. At $Re = 40$ k before and after the low-to high-lift transition, the wing tip deflection $z'/c \approx 0.11$ %. At $Re = 60$ k, a difference in wing tip deflection is observed when SI-SII transition occurs. In the low-lift (SI) state, $z'/c \approx 0.2$ %, and after transition to the high-lift (SII) state, $z'/c \approx 0.07$ %. The difference is likely due to the increased influence of unsteady aerodynamic forces, which
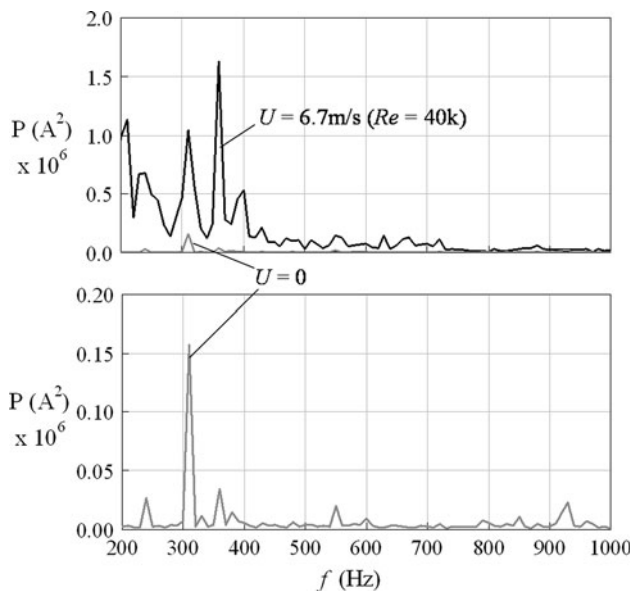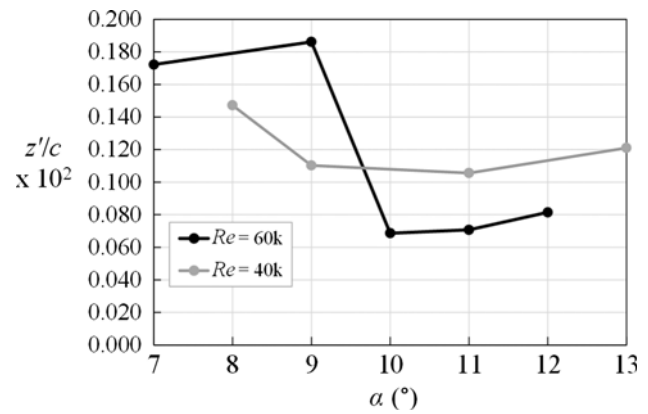

Fig. 4 Wing tip deflections normalized by the chord (z'/c) at $Re = 40$ and 60 k for the wing with all holes closed (i.e., *solid* wing)

are not resolved in this experiment, but are implied by the variations in spanwise vorticity, to be shown later.

2.4.3 Surface roughness

Surface roughness of sufficient height can act as a boundary layer trip, and wings with different roughness can act as though they operate at different Re. The nontrivial effect in flow separation and transition at these Re has been well documented [15]. The surface roughness near the wing tip ($y/b \approx -0.99$) was measured at different points along the chord by a Ambios Technology XP Stylus Profiler with a vertical resolution of 1.5×10^{-9} m. For a given chordwise 5-mm segment, multiple scans were made where each data set consisted of 37,300 points. A 5th-order polynomial curve was fit to each data set and removed to obtain the relative, small-scale surface roughness. At $x/c \approx 0.3$, where the wing is visibly and tangibly the smoothest, the maximum measured roughness height h_r was 6.3 microns. At $x/c \approx 0.9$, where the wing is the roughest, the maximum measured $h_r \approx 15$ microns. The roughness may be compared with the likely boundary layer thickness, δ, which for a flat plate at zero incidence is

$$\delta = 5\sqrt{\frac{xv}{U}}, \tag{1}$$

where x is the distance from the leading edge. At $x/c = 0.3$, $\delta = 1.3$ mm, and $h_r/\delta = 5 \times 10^{-3}$. At $x/c = 0.9$, $\delta = 2.1$ mm, and $h_r/\delta = 0.01$. The surface roughness is small compared with a boundary layer thickness.

We will be considering the effect of small cavities of 0.5 mm diameter, which could also be argued to be acting as roughness elements. However, the roughness is also a small fraction of the cavity diameter, 1.3 and 3 % at the smoothest and roughest points on the wing, respectively. Since the hole geometry is at least two orders of magnitude larger than the surface roughness, its effect can be clearly

Fig. 3 Acoustic power spectra in an empty wind tunnel with flow at $U = 6.7$ m/s ($Re = 40$ k) and without flow. Note the change in axis scales

distinguished, from the small-scale distributed manufacturing roughness. Subsequent tests described later will isolate the geometric surface and volumetric effects.

3 Results

3.1 Open holes on the suction surface

Figure 5 compares the aerodynamic performance at $Re = 40$ and 60 k of the baseline solid wing and a second wing with the same geometry except for the presence of the arrays of 0.5-mm-diameter holes. At $Re = 40$ k, the baseline wing has the characteristic jump from SI to SII at $\alpha = 12°$ (Fig. 5a, b). This transition is marked by an increase in C_L from 0.7 to values above 1, and a reduction in drag coefficient by about 10 %. At $Re = 60$ k, the jump from SI to SII occurs at $\alpha = 9°$ (Fig. 5c, d), with similar C_L increase and drag reduction. The wing with holes (also referred to as the perforated wing) has no such transition and is in the upper lift state, SII, at all α. Consequently, before the SI-SII transition for the baseline wing ($0° \leq \alpha \leq 12°$ at $Re = 40$ k and $0° \leq \alpha \leq 9°$ at $Re = 60$ k), the perforated wing has a higher efficiency, as measured by L/D, than the baseline case. The performance improvement is entirely passive, with no active energy input.

3.2 Surface geometry and cavity flows

A comparison was made between two cases where the holes were covered differently. In one case, the holes were filled and sealed with modeling clay, and in the other case, the holes were covered and sealed at the underside of the lid so that each hole became a cavity with aspect ratio $w/h = 1/2$. The resulting forces on the wing for the two cases show that a wing populated with small, sealed cavities performs just as though the cavities were absent, which is the same as the baseline wing (Fig. 6). Any effect of the unsealed cavities on the flow depends upon the presence of the backing cavities, and the holes in the surface themselves do not act like roughness elements (unsurprisingly given their size, as previously noted), and their geometry alone does not appear to generate secondary fluid flows that then affect the boundary layer separation and/or reattachment.

3.3 Chord location

The SI–SII transition is accompanied by a forward chordwise movement of the mean separation line. The early separation leaves sufficient time, in fractions of (c/U), so that transition to turbulence and reattachment can occur. Chordwise local disturbances could effectively promote this transition, and this concept was tested by leaving open

Fig. 5 Effect of open holes on the aerodynamic performance of an E387 wing at $Re = 40$ k (**a**, **b**) and 60 k (**c**, **d**)
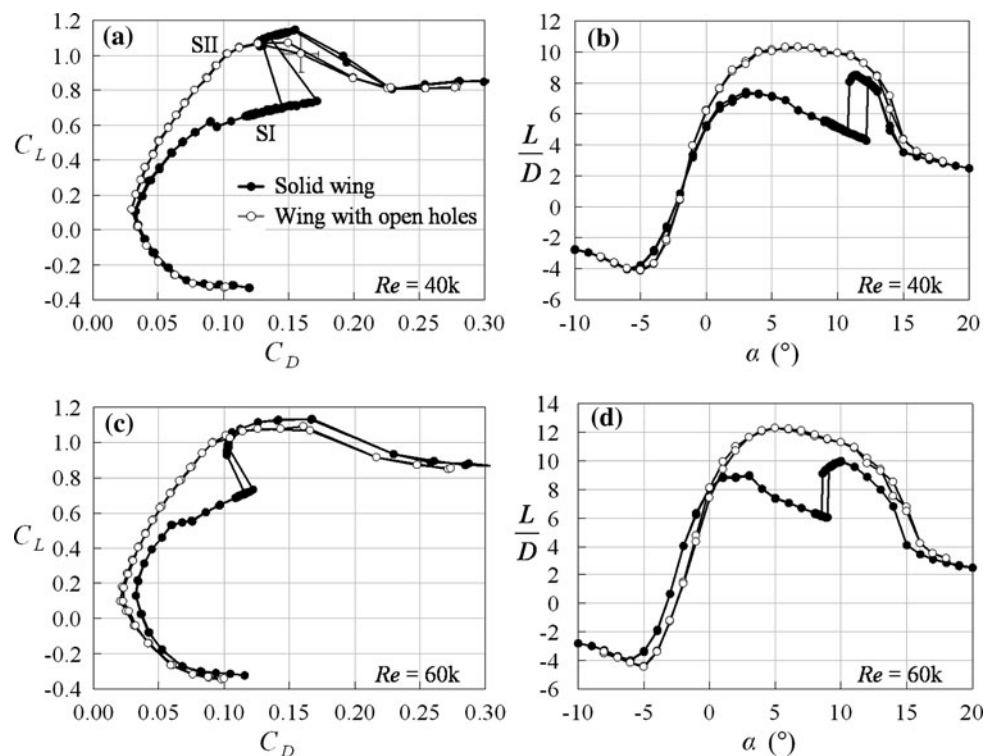
Fig. 6 Small surface cavities have no effect on wing performance ($Re = 40$ k)
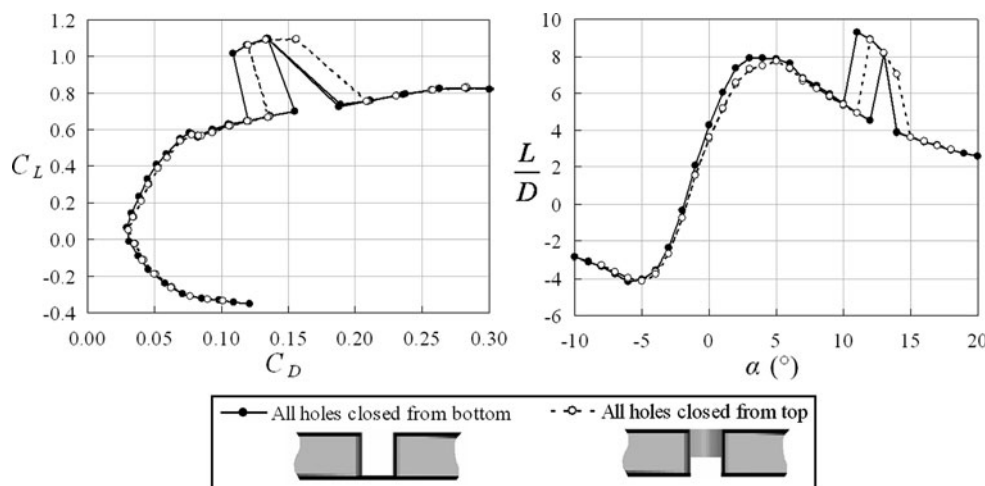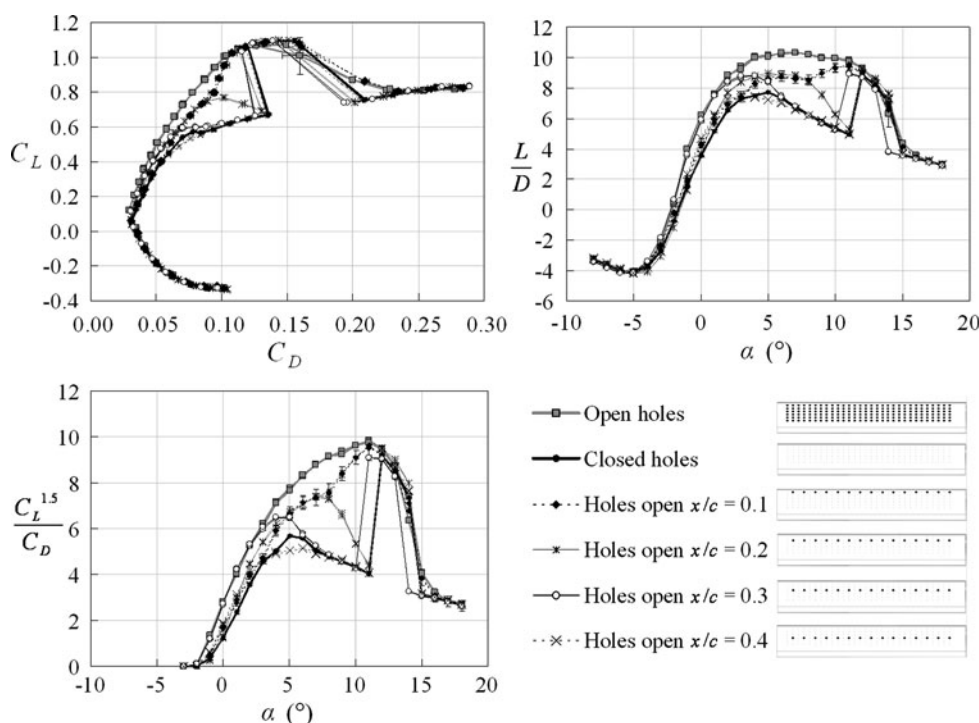

Fig. 7 Single rows of holes at varying x/c allow the envelope of performance curves to be populated between SI and SII at $Re = 40$ k

individual spanwise rows of holes at a given x/c location, while closing all others. For a row with open holes, 15 holes spaced 3.2 cm apart ($\Delta y/b = 0.12$) were left open across most of the span ($-0.83 \leq y/b \leq 0.83$). The $C_L(C_D)$ and L/D curves for the wing with selected rows of open holes located at $x_o = x/c = 0.1, 0.2, 0.3, 0.4$ are shown in Fig. 7 ($Re = 40$ k) and Fig. 8 ($Re = 60$ k).

For both Re cases, single rows of open holes at specific chord locations allow the envelope of $C_L(C_D)$ and (L/D) (α) to be populated with results that are intermediate between the extremes where all holes are open or all closed. As the row location moves closer to the leading edge, the performance curves are pulled toward the SII state, as generated with all holes open. When $x_o = 0.1$, there is no

abrupt jump in either L or D and the curves lie close to SII over all α. At $Re = 40$ k, the curves once again show sharp jumps between states when $x_o \geq 0.2$, and for $x_o \geq 0.3$, the performance curves are much closer to, though still measurably improved upon, the original solid baseline wing. At $Re = 60$ k, the curves show the sharp jumps when $x_o \geq 0.3$.

3.4 Open and closed exit port

The original design of the wing included two exit ports at the right wing tip, which were meant to be used for electrical connections. The results shown in Figs. 5, 6, 7, and 8 were for the wing with open exit ports. Figure 9 shows the L/D curves for the wing with different rows of open holes

Fig. 8 Similar variation in performance curves between SI and SII occur for different rows of open holes at $Re = 60$ k
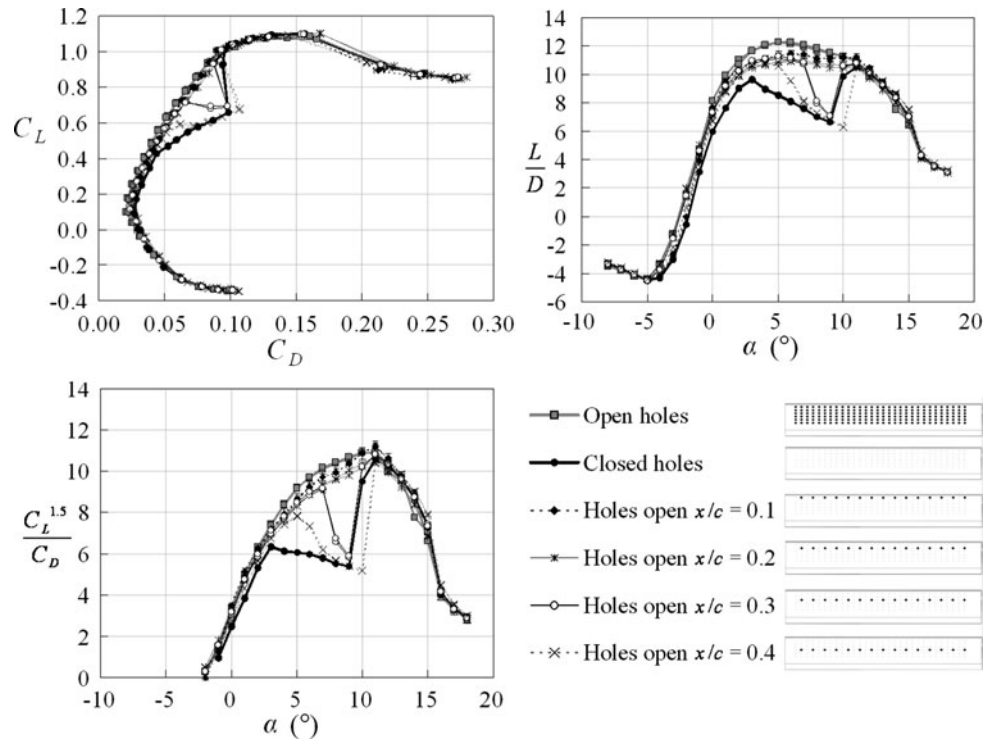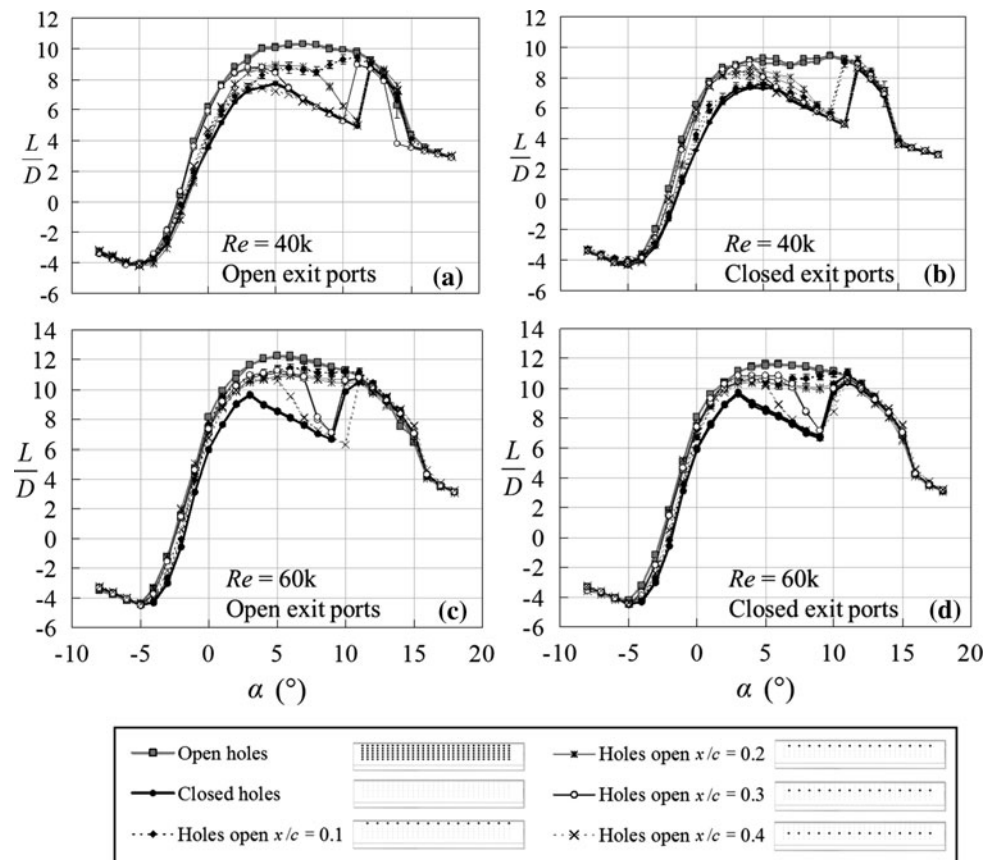

Fig. 9 L/D for different spanwise rows of open holes with open and closed exit ports at $Re = 40$ k (**a, b**) and $Re = 60$ k (**c, d**)

with *closed* exit ports at $Re = 40$ and 60 k. At the lower Re (Fig. 9a, b), the family of curves crossing from SI to SII is restricted to $\alpha \leq 7°$ in the pre-stall regime. If the effect of the holes is to trigger separation (and then re-attachment) toward the leading edge, then they are less effective when the large cavity volume is closed off. This phenomenon does not occur, however, at the higher Re, where the curves are nearly the same for both open and closed exit ports (Fig. 9c, d). While the effect of opening and closing the exit port affects the performance at the lower Re, this variation was not pursued in further detail. The remaining results were obtained with open exit ports.

A possible reason for the performance improvements from the open holes is acoustic resonance in the chambers that back them. If the resonant acoustic modes are in the appropriate frequency range, then intrinsic flow instabilities could be amplified as the acoustic waves impinge upon the boundary layer or separated shear layer.

3.5 Acoustic measurements

In this experimental setup, it is not straightforward to insert a measurement probe into the flow while leaving the sensitive SI–SII transition unchanged. In tests on a same-sized E387 wing under acoustic excitation at similar Re and pre-SI-SII transition α [28], the placement of a microphone near the top surface of the wing prevented the flow from reattaching when it otherwise normally would, thus keeping the flow in SI.

Since the characteristics of SI–SII transition can be monitored here, one can search for arrangements where it is not affected by the microphone presence. As an example check on possible feedback from the presence of the microphone to the wing, power spectra were taken with the microphone placed at different distances from the wing surface (in the z-direction) at $y/b = 0$ and $x/c = 0.1$. Examples measured above the wing with open holes at $x/c = 0.1$ and closed exit port are shown in 10. By monitoring the SI–SII state through jumps in the overall lift force, an adequate distance between the tip of the microphone nose cone and the wing surface was determined to be $z/c = 0.15$, and all subsequent power spectra were obtained with the microphone placed at that location.

The power spectra at $Re = 40$ k are shown in Fig. 11 for no wing (a), wing with open holes at $x/c = 0.1$ and closed exit port (b), wing with open holes and open exit port (c), and holes covered (d). For cases (b)–(d), $\alpha = 10°$. When the holes are closed (Fig. 11d) and when the holes are open at $x/c = 0.1$ with closed exit ports (Fig. 11b), the wing is in SI (corresponding to Fig. 9b), and the power spectra have a peak at $f = 600$ Hz for these two cases. This value of 600 Hz is later shown to match an experimentally measured vortex

passage frequency above the wing surface. When holes are open at $x/c = 0.1$ with *open* exit ports (Fig. 11c), the wing is in SII (corresponding to Fig. 9a), and the power spectrum has no peak at $f = 600$ Hz. A natural frequency of 600 Hz occurs over the wing in SI, but once the wing is in SII, it is no longer measurable in the external flow field. Similarly, the 400 Hz peak, which is highest when the wing is in low-lift SI, is reduced in amplitude when the flow is controlled to state SII, and it could mark a harmonic of a flow instability frequency that is suppressed in the presence of control.

3.6 Cavity volume

The preceding results suggest that the aerodynamic improvements in Fig. 5 could be caused by pressure fluctuations within the cavities and corresponding velocity fluctuations at the orifices due to acoustic resonance. If this is so, then varying the cavity volume/geometry should affect the resonant frequencies in predictable ways. In the original wing design, the cavities were not fluid-dynamically isolated from each other, as shown by the schematic in Fig. 12, but this base topology could easily be changed.

The performance of the wing at $Re = 40$ k was analyzed when the holes in the lid were left open, but the cavities were isolated from each other so that each hole communicated only with its own local chamber, or reservoir. Figure 13 shows that the isolated cavity model behaves similarly as the original perforated wing, being in SII at positive α. However, in the range $0° \leq \alpha \leq 12°$, L/D values for the wing with isolated cavities are slightly lower than for the wing with connected cavities. Topologically, the isolated cavity model is the same as the $AR = 1/2$ sealed holes. The difference lies only in the volume of the cavity.

For a single row of open holes located at $x/c = 0.1$, lift and drag forces were compared for two different internal cavity volumes. Part of the volume directly below the holes was reduced by approximately 24 %. The resulting $C_L(C_D)$ and L/D curves at $Re = 40$ k are shown in Fig. 14. The reduced cavity volume case yields a slightly lower L/D curve between $-4° \leq \alpha \leq 12°$. A decrease in performance in the same α range was also observed at $Re = 60$ k.

3.7 Spanwise variation

The influence of spanwise uniformity of the open holes was examined. In Figs. 5, 6, 7, 8, 9, 10, 11, 12, 13, and 14, open holes spanned from $-0.83 \leq y/b \leq 0.83$. At $x/c = 0.1$, only nine holes centered at mid-span ($-0.48 \leq y/b \leq 0.48$) were left open, while all those closer to the wing tips were closed. Partial coverage with open holes at mid-span (Fig. 15) generates lift-drag polars and $(L/D)(\alpha)$ curves that are intermediate between
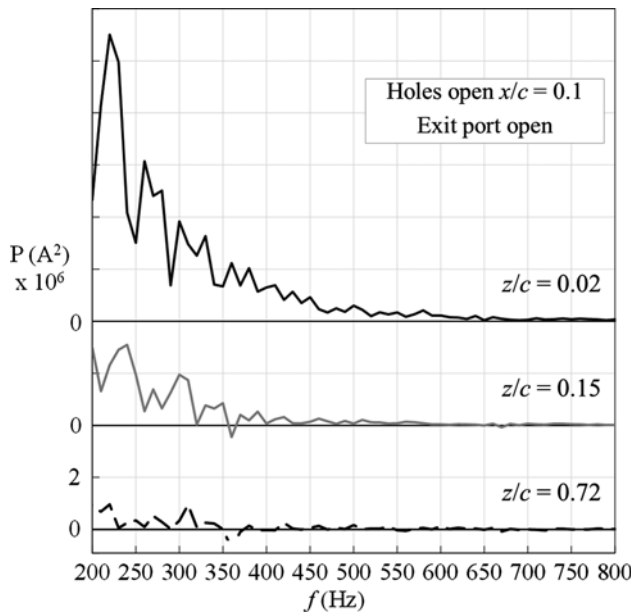
Fig. 10 Power spectra at $Re = 40$ k and $\alpha = 10°$ for the wing with open holes at $x/c = 0.1$ and open exit port measured at various distances, z/c, from the *top* surface

those of fully closed and fully open holes. The intermediate curves still show sharp SI–SII transitions.

The intermediate result suggests that the integrated force on the whole wing can be controlled by spanwise variation of local conditions. Figure 16 provides further support. The figure shows example of short-time-averaged spanwise vorticity fields from five spanwise planes under the same conditions. The sections are at $y/b = \{0.0, -0.15, -0.30, -0.44, -0.59\}$. The first location (station #1) is at mid-span, directly at an open hole location. Here, and in the next two neighboring locations, a large leading edge separation bubble is followed by reattachment shortly after mid-chord. The reattached flow corresponds locally to state SII. The last two stations at $y/b = \{-0.44, -0.59\}$ lie either side of an open hole, but both show a short separation bubble that does not reattach. The effective separation point is much closer to the leading edge and the wake is much wider. This flow state corresponds to SI. The flow at station #4 is controlled not only by the most proximate hole state, but also by the flow in adjoining station #5. Raw particle images show the changes in the geometry of the separation line, which is darker than the surrounding particle-laden areas. At $y/b = -0.15$ (station #2), the dark separation line remains close to the suction surface with small dark regions marking concentrations of spanwise vorticity, which move down the wing, consistent with structures seen on the left panels. This is a locally attached (SII) flow. At $y/b = -0.59$ (station #5),
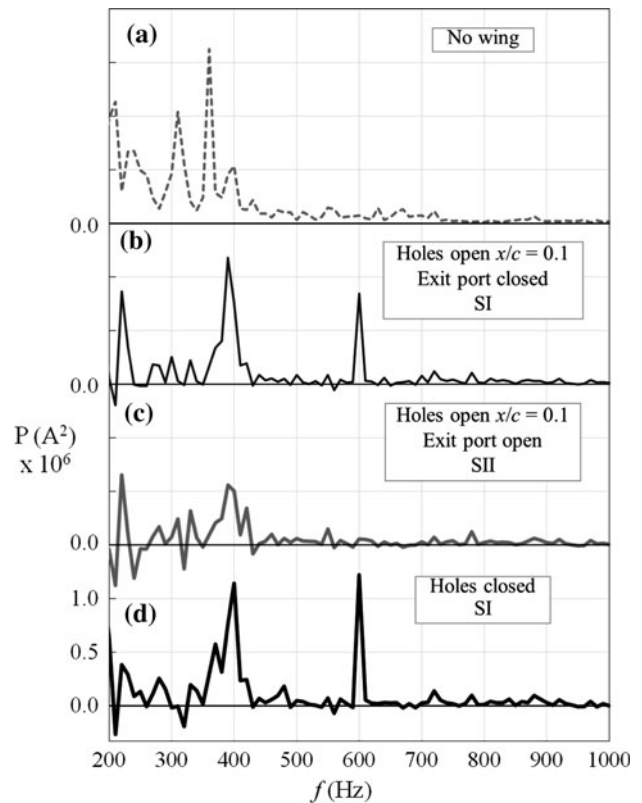

Fig. 11 Power spectra at $Re = 40$ k. **a** No wing; **b** wing with closed holes; **c** wing with open holes ($x/c = 0.1$) and open exit port; **d** wing with open holes ($x/c = 0.1$) and closed exit port. For **b–d**, $\alpha = 10°$
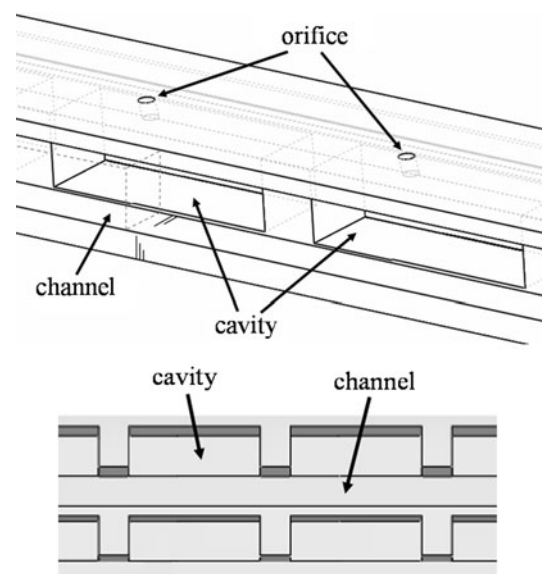

Fig. 12 Schematic of cavities interconnected by a channel. Each cavity was designed to house speakers with an adjacent channel for wiring

the separation line clearly departs from the suction surface just before mid-chord, corresponding to a locally separated (SI) flow.

Fig. 13 $C_L(C_D)$ (*left*) and L/D (*right*) for a E387 wing at $Re = 40$ k with closed holes, open holes and open holes with isolated cavities
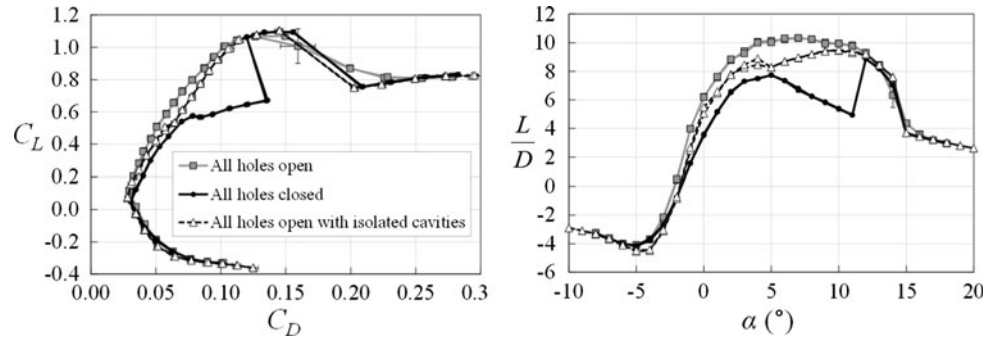
Fig. 14 $C_L(C_D)$ (*left*) and L/D (*right*) for a E387 wing with 15 open holes at $x/c = 0.1$ and two different internal cavity volumes
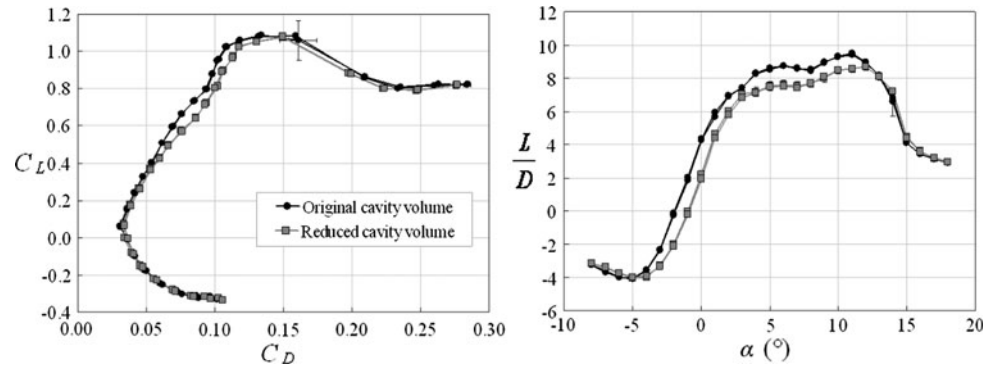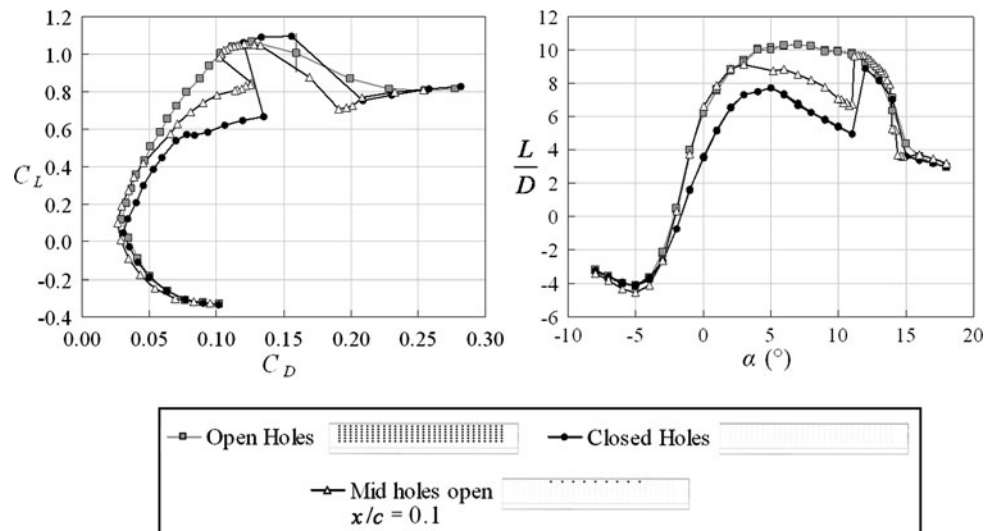
Fig. 15 $C_L(C_D)$ (*left*) and L/D (*right*) for a E387 wing at $Re = 40$ with mid-portion holes open ($-0.48 \leq y/b \leq 0.48$) at $x/c = 0.1$

4 Discussion

On a wing that is characterized by abrupt jumps in lift and drag coefficient between what we have termed SI, where the flow separates at some point between mid-chord and the trailing edge, and SII, where separation close to the leading edge is followed by reattachment, the dynamics are very sensitive to a number of different perturbations. In a study originally aimed at acoustic forcing of the flow, it was found, quite by accident, that the presence of the holes themselves in the wing suction surface was sufficient to affect the global behavior. When holes are present, the flow state switches from SI to high-lift SII, with no other control input necessary. The mechanism is entirely passive, and a control strategy might simply involve sliding lids open and shut to modify local flow characteristics.

The effect on the wing is approximately local, so that chordwise strips can affect local sectional c_l and c_d. Since each local flow state is either in SI or SII, one may think of the wing as a device whose lift and drag coefficients can be manipulated under digital control. Local states can be on or off, and asymmetries across the span will lead to rolling

Fig. 16 Spanwise vorticity fields $\omega_z(x, z)$ are averaged over 20 independent samples to give a map whose strongest features are steady, but an indication of the unsteady structure remains. This is superimposed on similarly time-averaged fluctuating velocity vector fields at spanwise sections $y/b = 0.0$, -0.15, -0.30, -0.44, -0.59 for the E387 at $Re = 40$ k and $\alpha = 11°$ with open holes at $x/c = 0.1$ and $0.48 \leq y/b \leq 0.48$. Every third vector is plotted. Raw PIV images at $y/b = 0.0$, -0.15 show dark separation lines that distinguish between locally attached and locally separated flow
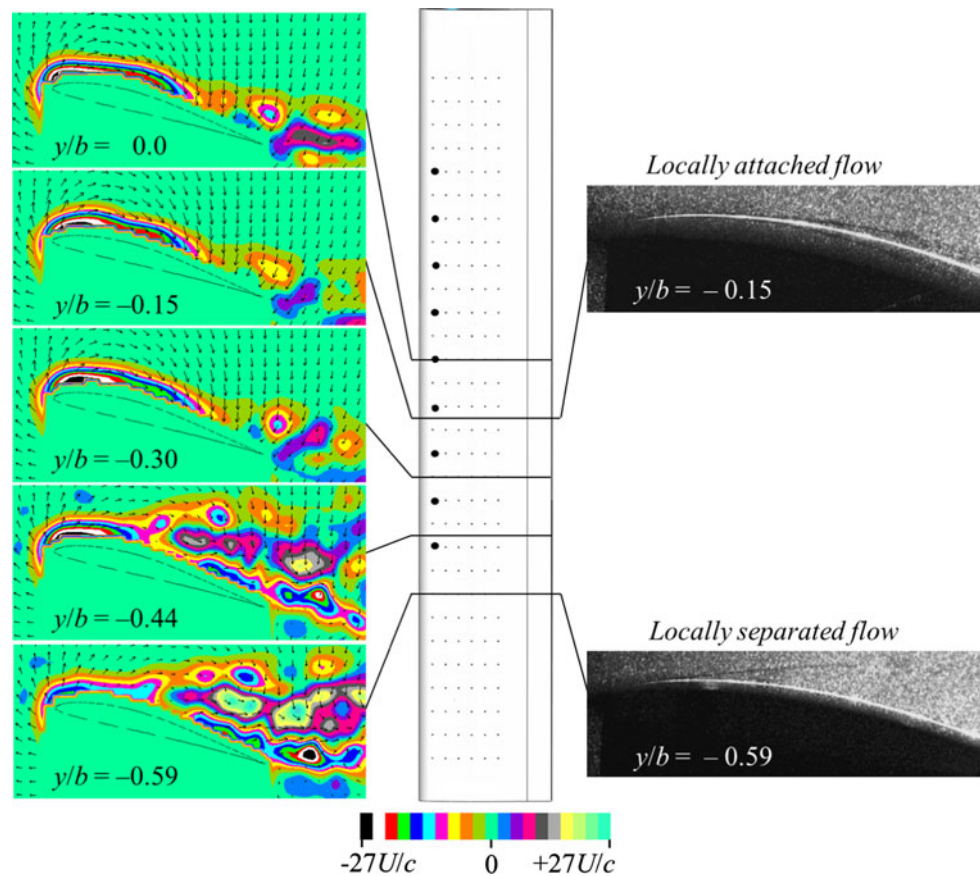
moments, while symmetrically (about mid-span) actuated hole opening can yield pre-determined total lift and drag from the envelope of possibilities.

4.1 Surface geometry and cavity flows

The performance characteristics of the perforated wing could be due to some form of cavity flow. In general, cavity flow can be categorized into three main types, as detailed in [20]: (a) fluid-dynamic, where oscillations come from the instability of the cavity shear layer and are enhanced through a feedback mechanism, (b) fluid-resonant, where oscillations are strongly coupled with resonant (standing) wave effects, and (c) fluid-elastic, where oscillations are linked to solid boundary motion. It is also possible to have combinations of different types of cavity flow.

In purely fluid-dynamic cavity flow, the feedback mechanisms that enhance the oscillations are driven by the presence of the cavity downstream edge [20]. This type of cavity flow includes the flow over a cavity covered by a perforated plate, whose uses include acoustic lining for sound attenuation [14]. In studies on the shear layer oscillations along a perforated plate backed by a cavity [3],

the predominant frequency varied with impingement length and inflow velocity. Without the perforated plate, the shear layer was separated with an inflection point, while with a perforated plate, the shear layer was bounded with no inflection point. It was also suggested in [4] that unified, large-scale motion occurs through the plate perforations and induces jet flow at the downstream end of the perforated plate. The long-wavelength instabilities along a perforated plate of length L can be expressed as a Strouhal number, fL/U, where f is a shedding or oscillation frequency. The reported values of fL/U are on the order of 0.5–0.6 [8]. If the chord of the wing is used as an effective plate length, the calculated $fL/U \approx 8$ is an order of magnitude larger.

In classical cavity flows, the cavity length must be several times larger than a boundary layer thickness at the upstream lip in order for amplification to occur in the instabilities in the cavity shear layer. Estimates of δ from Eq. (1) ranged from about 1–2 mm along the chord, which are always larger than the streamwise cavity length of 0.5 mm. Moreover, in the current tests, a cavity of finite depth (equal to twice its diameter), by itself, has no effect on the performance of the wing. Changes in flow occur

only when the holes are connected to a larger chamber and when the chamber volume is varied, suggesting the presence of acoustic resonance effects.

4.2 Helmholtz resonance

Fluid-resonant cavities include Helmholtz resonators, which are distinguished by the very large ratio of cavity volume to cavity orifice area [20]. In general, a Helmholtz resonator is a device in which a volume of compressible fluid is enclosed by rigid boundaries with a single small opening and can be modeled by a second-order mass-spring system where the fluid in the orifice has an effective mass and the compressibility of the fluid in the chamber is the stiffness [19]. The resonator has a natural frequency, and when the instabilities in the flow match the natural Helmholtz frequency, flow-excited resonance occurs. In such cases, small pressure disturbances can produce large velocity fluctuations at the orifice and large pressure fluctuations inside the resonator [19].

The Helmholtz resonant frequency is

$$f_H = \frac{a}{2\pi}\sqrt{\frac{\kappa}{V}}, \tag{2}$$

where a is the speed of sound, κ is a quantity that represents the resistance of fluid passage through the orifice, and V is the cavity volume [27]. For a circular orifice, the resistance is

$$\kappa = \frac{\pi r^2}{h + 1.697r}, \tag{3}$$

where r is the orifice radius, and h is the orifice thickness (neck height) [27].

For multiple orifices in a single cavity, the resistance terms can be summed, yielding a resonant frequency

$$f_H = \frac{a}{2\pi}\sqrt{\frac{\kappa_1 + \kappa_2 + \cdots}{V}}. \tag{4}$$

Equations 3 and 4 were used to calculate the Helmholtz resonant frequency for a single spanwise row of 15 open holes with interconnected cavities (Fig. 14). The combined cavity and channel volume is approximately 14,200 mm^3 Solving for f_H yields $f_H = 650 \pm 3$ Hz, where the uncertainty comes from the uncertainty in cavity and channel volume measurements. An instability frequency can be estimated from the properties of the vortical structures above the wing,

$$f_i = \frac{U_a}{x_s}, \tag{5}$$

where U_a is the streamwise advection speed, and x_s is the average separation between vortices, as observed in PIV data (e.g., Fig. 17). At $Re = 40$ k and $\alpha = 10°$ for the case
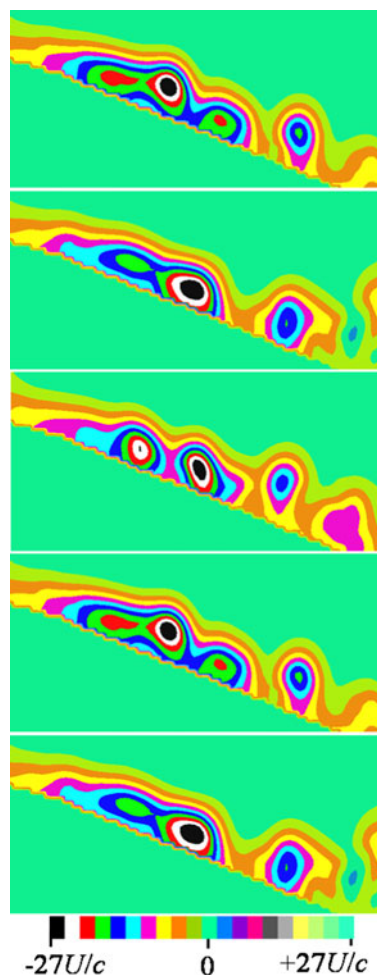

Fig. 17 Instantaneous spanwise vorticity fields over the aft portion of the wing (beginning at $x/c = 0.5$) at $Re = 40$ k and $\alpha = 10°$ with 15 open holes at $x/c = 0.1$. The time between successive vorticity fields is 0.1 s

of 15 open holes at $x/c = 0.1$, the calculated instability frequency is $f_i = 630 \pm 90$ Hz, where the uncertainty comes from using different pairs of neighboring vortical structures and the uncertainty in locating the vorticity centers. The calculated f_i is equal to the calculated f_H For the reduced volume case where the volume is approximately 10,800 mm^3 (Fig. 14), the calculated Helmholtz resonance is $f_H = 750 \pm 3$ Hz. The calculated instability frequency is $f_i = 730 \pm 50$ Hz, which again equals f_H.

The calculation of f_H in Eq. 2 is independent of flow speed. For a given resonator volume and orifice radius, the same resonant frequencies should be generated for varying flow speeds. This was confirmed by calculating f_i at $Re = 60$ k and $\alpha = 8°$ for the case of 15 open holes at $x/c = 0.1$. For the original volume, $f_i = 650 \pm 90$ Hz, and for the reduced volume, $f_i = 710 \pm 50$ Hz, which are equal to the values of f_i at $Re = 40$ k for the two different volumes, respectively.

When the number of open holes is doubled from 15 to 30 (while keeping all other parameters the same), the calculated Helmholtz resonance is $f_H = 925 \pm 3$ Hz. At $Re = 60$ k and $\alpha = 8°$, the calculated instability frequency is $f_i = 830 \pm 100$ Hz. The large variation could be due to the fact that the interconnected cavities might not truly act as a single large cavity, but rather a series of small cavities. In the example given in [27], when two resonators are connected together in series, one of the resonators can experience a slightly different resonant frequency depending on the geometry of the connecting channel between the two resonators. In the same example, if one of the cavities is open to the atmosphere, then the resulting resonant frequency can be as much as a factor of 2.4 different than a simple resonator [27]. For the current wing, opening and closing the exit ports yielded different results, which were especially prominent at the lower Re. The ratio of the calculated f_i for open and closed exit ports at $Re = 40$ k is $f_{i,\text{open}}/f_{i,\text{closed}} \approx 2$.

Since the power spectra in Fig. 11 were measured at $x/c = 0.1$, and separation occurs at $x/c = 0.2$, $f = 600$ Hz most likely matches a readily amplified frequency that grows first in the still-attached boundary layer, and then subsequently after separation. The peak in power spectra at $f = 600$ Hz disappears when the flow is reattached and the wing is in SII. 600 Hz is close to the calculated f_H and equal to f_i, suggesting that a matching of the Helmholtz resonance with the naturally occurring instability frequency in the boundary layer promotes flow reattachment and SI–SII transition. Once this frequency matching occurs, the reattached SII shear layer contains structures like those in Fig. 17 that propagate with the initial SI separated boundary layer frequency, which is equal to the Helmholtz resonant frequency.

For airfoil shapes, such as the E387, that exhibit distinct jumps between the SI and SII states at transitional Re, the same Helmholtz resonant frequencies in perforated wings can be expected over the entire Re range and should yield similar results as this study at $Re = 40$ and 60 k. Key parameters that change the resonant frequency are orifice radius, orifice neck height and cavity volume. Additional parameters such as the number of orifices and connecting channel geometry need to be considered when the resonator is more complicated, as in the case of the current perforated wing.

4.3 Similarities to woodwind instruments

Helmholtz resonance is the primary means for how many woodwind instruments work, such as the ocarina or a transverse flute. The distinct frequencies of woodwind instruments depend on various parameters, including instrument size and geometry, selection of open and closed finger holes, finger hole size and spacing, type of mouthpiece, and even the angle at which the air flows over the mouthpiece. Extensive details can be found on the physics and design of woodwind instruments (e.g., [1, 2, 6, 11]), and the main sound production mechanism that governs woodwind instruments similarly governs the perforated wing.

The semi-porous wing in the current study contains numerous combinations of open and closed holes along different spanwise and chordwise arrays, similar to the finger holes on a woodwind instrument, if the wing is much like an ocarina when the exit port is closed, and a transverse flute when the exit port is open. However, the wing has no single mouthpiece or embouchure, but rather spanwise rows of embouchures that can be blown across simultaneously.

It should also be noted that f_H in Eq. 2 is independent of cavity geometry, which explains why ocarinas can be made into so many different shapes, as long as the internal volume is controlled. The orifice geometry of Helmholtz resonators was shown in [5] not to be a significant factor in the resulting resonant frequencies. In the current study, the intricate interior design of the wing makes the wing a more complicated resonator that may require different mathematical formulations to obtain the precise resonant frequencies for various combinations of open and closed holes, angle of attack, etc.

In [28], a solid E387 wing at $Re = 40$ k was acoustically excited by an external sound source. At excitation frequencies from the sound source that matched tunnel anti-resonances (415, 520 and 660 Hz), the wing experienced an almost 80 % increase in L/D. One of the optimum excitation frequency values (660 Hz) matches the calculated f_H for the perforated wing. The calculated values of f_i, also obtained from the PIV data, are the second harmonics of the excitation frequencies, f_e. Results from [28] indicate that the flow over the wing is altered when external acoustic excitation induces maximum fluctuating velocities on the wing (at tunnel anti-resonances). Minimum pressure and maximum velocity also occur at the embouchure of a flute, where the air flow occurs [7]. The current study suggests that the open holes act similarly to embouchures for Helmholtz resonators that amplify the natural frequency of the fluid instabilities through traveling acoustic waves. That contrasts with external acoustic excitation, where the most amplified frequency is driven by the matching of acoustic frequencies with *standing* waves setup by tunnel resonance. Here, the traveling acoustic waves from the Helmholtz resonators induce pressure fluctuations at the orifices that propagate into the separated shear layer immediately above. The perforated wing shares some characteristics with woodwind instruments and may be thought of as a type of multi-embouchure woodwind instrument that uses a combination of cavity resonance and

Fig. 18 Typical pressure tap geometry (schematic adapted from [12]) has the essential components of a Helmholtz resonator
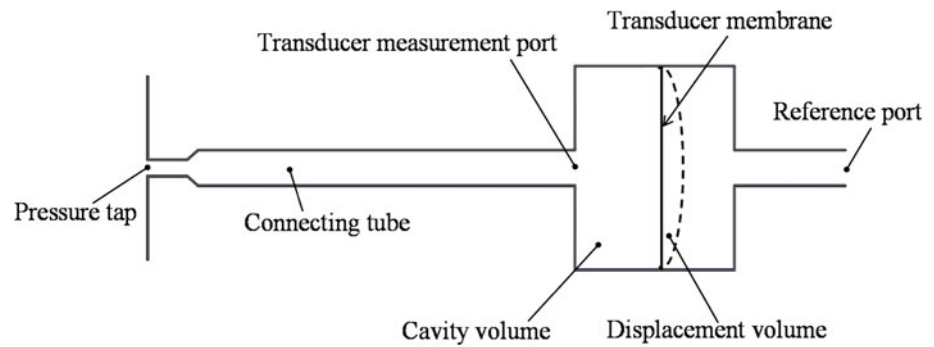
pipe flow to alter the nominal characteristics of the boundary and separated shear layers.

4.4 Pressure tap measurements

There are certain practical implications of these results. One is that if airfoils and wings are instrumented with pressure taps in this transitional regime, then their chamber volumes must be carefully selected to remove resonant frequencies from possible interactions with the intrinsic flow instabilities, or those induced at the orifice opening. A typical pressure tap is connected by a tube to a pressure transducer, which contains a cavity, as shown in the schematic in Fig. 18. In a multiple-pressure tap setup, the connecting tubes are typically connected to a scanning valve which then connects to the transducer. The pressure tubes can vary in length depending on the placement of the pressure taps in the wing model, but essentially a pressure tap setup closely resembles a Helmholtz resonator.

Calculations of f_H from Eqs. (2) and (3) can be made for different tube lengths (neck heights), h, assuming constant orifice/tube radius, or constant cavity volume. Assuming an orifice radius (equal to tube radius) of 0.5 mm, and setting the cavity volume to those for three models of Validyne pressure transducer (DP15, DP303 and Type 45-14), yields the curves in Fig. 19a. Alternatively, setting the cavity volume to that of the Type 45-14, while varying the orifice diameter (tube radius), gives the curves in Fig. 19b.

f_H calculated here gave resonant frequencies between 600 and 950 Hz. In the acoustic studies reported in [28], excitable frequencies that cause SI-SII transition at $Re = 60$ k range between 400 and 1,000 Hz. Figure 19 suggests that using pressure transducers with smaller cavity volumes and/or having smaller orifice/tube radii may be problematic for tube lengths less than about 14 cm. This could happen when the pressure transducers are located directly inside the wing, which results in shorter tube lengths. Longer pressure tubes (greater than 20 cm) seem to be safer in order to avoid resonance effects from pressure taps.

Given the similar configuration of a pressure tap system to a Helmholtz resonator, the presence of pressure taps may
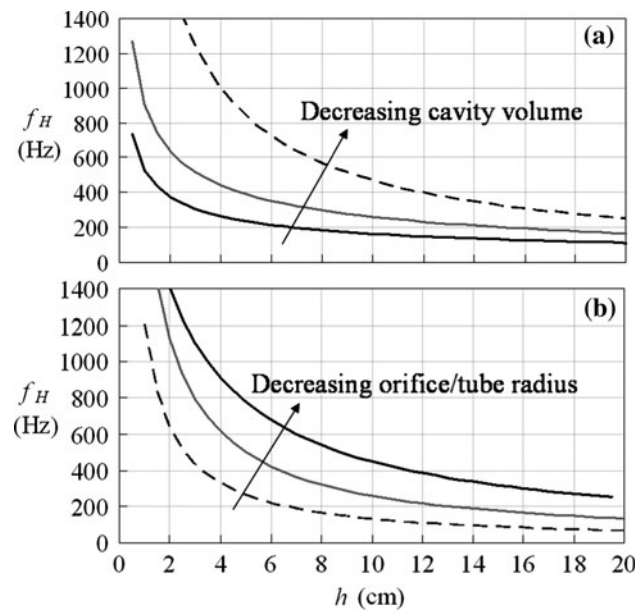
Fig. 19 Relationship between Helmholtz frequency, f_H, and tube length (neck height), h, for constant orifice/tube radius and variable cavity volume (**a**), and for constant cavity volume and variable orifice/tube radius (**b**)

modify the flow over a wing, preventing SI–SII transition. The flow will also then be nonuniform and forced at spanwise scales set by the pressure tap spacing. For example, data on the E387 airfoil in the same Re regime [18] included sectional pressure coefficients, obtained by 129 0.5-mm-diameter pressure orifices on the wing surface. The data show significant spanwise variation in c_d at $Re = 100,000$, and the lowest values of c_d were measured at the location of the pressure taps. These findings parallel those from the current study, which show higher C_L and lower C_D for configurations with open holes (Figs. 5, 7, 8, 9, 15). The local sectional flow state (SI or SII), local wing circulation and section drag have been shown to be correlated for the E387 wing in this Re regime [29]. Here, it is clear that the presence of open holes induces spanwise variation in wing circulation and hence section drag coefficient.
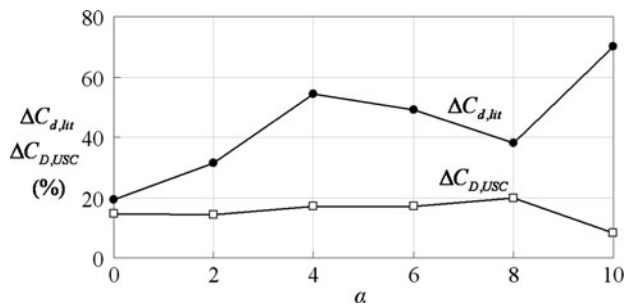
Fig. 20 $\Delta C_{d,\text{lit}}$ for the E387 airfoil at $Re = 60$ k among different facilities [22], and $\Delta C_{D,\text{USC}}$ between open and closed holes for the E387 wing at $Re = 60$ k

Measured lift and drag coefficients for the E387 vary widely throughout the literature, especially at lower Re. The relative difference in measured c_d for the E387 airfoil at $Re = 60$ k among different facilities [22] can be expressed as a fraction of the maximum c_d,

$$\Delta C_{d,\text{lit}} = \frac{c_{d,\max} - c_{d,\min}}{c_{d,\max}}. \tag{6}$$

The result is given in Fig. 20. The data include experiments in which some of the models had pressure orifices and some did not. The variation in C_D for the E387 wing from the current study at $Re = 60$k with all open holes and all closed holes is shown as

$$\Delta C_{D,\text{USC}} = \frac{\left| C_{D,\text{open}} - C_{D,\text{closed}} \right|}{C_{D,\text{closed}}} \tag{7}$$

and is also plotted in the same figure. The values of $\Delta C_{d,\text{lit}}$ are higher than the values of $\Delta C_{D,\text{USC}}$, but they are not orders of magnitude apart, unlike a similar measure derived from the natural spanwise variation tests in [29]. The disruptive effect of holes in pressure tap measurements upon the global flow properties could be a significant factor in the observed variations in the technical literature. We may note also that the same results here show that small geometric cavities by themselves do not affect wing performance, so, for example, surface mounted MEMS probes that have small cavities should not be problematic.

The large changes caused by small geometries promoting resonance at the orifices suggest that very slightly permeable wings could also operate permanently in the high-lift SII state. Little attention has yet been given to the effects of permeability in feathered wings of birds, for example.

5 Conclusion

In the initial stages of testing the response of an E387 wing to acoustic excitation, the presence of small holes in the suction surface of the wing was found to significantly change the overall aerodynamic performance. This discovery led to an independent study of the effects of open holes on the forces and local flow dynamics of the E387 wing at the transitional $Re = 40$ k where flow separation and reattachment determine whether the wing is in a low SI or high SII lift state, respectively. Switching from SI to SII can be promoted by forcing through acoustic resonance of the small chambers when their resonant modes are close to the most unstable modes in the original (hole-free) flow. The large effect of the small holes suggests that some caution is required in interpreting and designing pressure tap measurements in this transitional Re range. In principle, the passive effects of the holes+chambers ought to be replaceable through equivalent, local forcing through small, embedded sources. Either one could be used for local, digital control of forces and moments on the wing, but with active acoustic forcing through loudspeakers, the frequency is an independent control parameter, not depending on the cavity geometry, and this possibility will be investigated in the future.

References

1. Benade A (1967) Fundamentals of musical acoustics. Oxford University Press Inc., Oxford
2. Benade A, French J (1965) Analysis of the flute head joint. J Acoust Soc Am 37:679–691
3. Celik E, Sever A, Rockwell D (2002) Shear layer oscillation along a perforated surface: a self-excited large-scale instability. Am Inst Aeronaut Astronaut 14:4444–4447
4. Celik E, Sever A, Rockwell D (2005) Self-sustained oscillations past perforated and slotted plates: effect of plate thickness. Am Inst Aeronaut Astronaut 43:1850–1853
5. Chanaud R (1994) Effects of geometry on the resonance frequency of Helmholtz resonators. J Sound Vib 178(3):337–348
6. Coltman J (1968) Sounding mechanism of the flute and organ pipe. J Acoust Soc Am 44:983–992
7. Dickens P, France R, Smith J, Wolfe J (2007) Clarinet acoustics introducing a compendium of impedance and sound spectra. Acoust Aust 35:17–24
8. Ekmekci A, Rockwell D (2002) Self-sustained oscillations of shear flow past a slotted plate coupled with cavity resonance. J Fluids Struct 17:1237–1245
9. Fincham A, Delerce G (2000) Advanced optimization of correlation imaging velocimetry algorithms. Exp Fluids 29:13–22
10. Fincham AM, Spedding GR (1997) Low cost, high resolution dpiv for measurement of turbulent fluid flow. Exp Fluids 23:449–462
11. Fletcher N, Rossing T (1998) The physics of musical instruments, 2 edn. Springer Science+Business Media Inc., Berlin
12. Freeman L, Carpenter M, Rosenberry D, Rousseau J, Unger R, McLean J (2004) Use of submersible pressure transducers in water-resources investigations. In: Techniques of water resources investigations, 8-A3. U.S. Geological Survey

13. Grundy TM, Keefe G, Lowson M (2001) Effects of acoustic disturbances on low re aerofoil flows. In: Mueller TJ (ed) Fixed and flapping wing aerodynamics for micro air vehicle applications. American Institute of Aeronautics & Astronautics, Reston, pp 91–112

14. Guess A (2009) Calculation of perforated plate liner parameters from specified acoustic resistance and reactance. J Sound Vib 40:119–137

15. Lissaman P (1983) Low-Reynolds-number airfoils. Annu Rev Fluid Mech 15:223–239

16. Lyon CA, Broeren AP, Giguere P, Gopalarathnam A, Selig MS (1997) Summary of low-speed airfoil data, vol. 3. Soartech Publication, Virginia Beach

17. McArthur J (2007) Aerodynamics of wings at low Reynolds numbers Ph.D. thesis. University of Southern California

18. McGhee RJ, Walker BS, Millard BF (1988) Experimental results for the Eppler 387 airfoil at low Reynolds numbers in the langley low-turbulence pressure tunnel. NASA 4062

19. Morris SC (2011) Shear-layer instabilities: particle image velocimetry measurements and implications for acoustics. Annu Rev Fluid Mech 43:529–550

20. Rockwell D, Naudascher E (1978) Review—self-sustaining oscillations on flow past cavities. J Fluids Eng 100:152–165

21. Selig MS, CA L, Giguere P, Ninham C, Guglielmo J (1996) Summary of low-speed airfoil data vol. 2. Soartech Publication

22. Selig MS, Guglielmo JJ, Proeren AP, Giguere P (1995) Summary of low-speed airfoil data, vol 1. Soartech Publication, Virginia Beach

23. Simons M (1999) Aircraft aerodynamics. Special Interest Model Books Ltd

24. Somers D, Maughmer M (2008) Experimental results for the e 387 airfoil at low reynolds numbers in the penn state low-speed, low-turbulence wind tunnel. In: AHS specialists conference on aeromechanics

25. Spedding G, Rignot E (1993) Performance analysis and application of grid interpolation techniques for fluid flows. Exp Fluids 15:417–430

26. Spedding GR, McArthur J (2010) Span efficiencies of wings at low Reynolds numbers. J Aircr 47:120–128

27. Strutt JWS (1964) On the theory of resonance. In: Scientific papers, vol 1, pp 77–118

28. Yang S, Spedding G (2013) Separation control by external acoustic excitation on a finite wing at low Reynolds numbers. Am Inst Aeronaut Astronaut 6:1506–1515. doi:10.2514/1.J052191

29. Yang S, Spedding G (2013) Spanwise variation in wing circulation and drag measurement of wings at moderate Reynolds number. J Aircr 3:791–797. doi:10.2514/1.C031981

30. Zabat M, Farascaroli S, Browand F, Nestlerode M, Baez J (1994) Drag measurements on a platoon of vehicles. California partners for advanced transit and highways (path), institute of transportation studies. University of California Berkeley